

LITHOLOGIC MAPPING OF SILICATE ROCKS USING TIMS

A.R. Gillespie

Geology Group

Jet Propulsion Laboratory
California Institute of Technology
Pasadena, California 91109

ABSTRACT

Common rock-forming minerals have thermal infrared spectral features that are measured in the laboratory to infer composition. NASA now operates an airborne Daedalus scanner (TIMS) that collects six channels of thermal infrared radiance data (8 to 12 μm) that may be used to measure these same features for rock identification. Previously, false-color composite pictures made from channels 1, 3, and 5 and emittance spectra for small areas on these images have been used to make lithologic maps. In this article, central wavelength, standard deviation and amplitude of normal curves regressed on the emittance spectra are related to compositional information for crystalline igneous silicate rocks. As expected, the central wavelength varies systematically with silica content and with modal quartz content. Standard deviation is less sensitive to compositional changes, but large values may result from mixed rock types within a pixel. Amplitude varies with quartz content and also with admixture of vegetation. Compression of the six TIMS channels to three image channels made from the regressed parameters may be effective in improving geologic mapping from TIMS data, and these synthetic images may form a basis for the remote assessment of rock composition.

INTRODUCTION

Common rock-forming minerals have thermal infrared spectral characteristics that can be used to infer rock compositions and construct lithologic maps from remotely sensed images. The strongest spectral features lie between 8 and 10 μm and are attributed to the fundamental vibrations of Si-O [e.g., Hunt and Salisbury, 1974; Hunt, 1980]. These reststrahlen bands are most pronounced in quartz. Partial substitution of Al, Mg or other elements for Si in a wide range of silicate minerals results in changes in the width, depth and wavelength of the band, as well as changes in its fine structure [e.g., Lyon, 1965]. For example, reststrahlen bands for quartz (SiO_2) are centered near 8.6-9.2 μm ; for albite ($\text{NaAlSi}_3\text{O}_8$) at about 8.7-9.9 μm ; and for olivine ($(\text{Mg},\text{Fe})_2\text{SiO}_4$) at about 10.0-10.5 μm . Although rock spectra are not simple mixtures of mineral spectra, systematic differences in the emittance spectra of rocks do correspond to features in the spectra of the major constituent minerals. These differences are sufficient to produce distinct differences in the apparent temperatures measured remotely, at different wavelengths. Thus multispectral thermal measurements are a means of

assessing rock composition, and multichannel thermal infrared images are a means of extending this information regionally, to form a basis for lithologic maps [e.g., Vincent et al., 1972; Kahle and Rowan, 1980].

Recently, NASA has acquired a Thermal Infrared Multispectral Scanner (TIMS) that measures six channels of photon flux data in the spectral region $8\text{--}12 \mu\text{m}$ [Palluconi and Meeks, 1985]. Previously, TIMS data have been displayed as false-color pictures made from three of the six image channels, enhanced to emphasize emittance information [Soha and Schwartz, 1978; Gillespie et al., 1986]. This approach does not make use of information from the discarded image channels. In a different approach, thermal emittances may be calculated from each of the image channels and displayed as spectra [Kahle and Walker, 1984]. Although in this approach no data are discarded, the obvious advantages of photo-interpretation cannot be exploited because the data are no longer displayed as pictures. If the emittance images themselves are displayed as false-color pictures, then three channels must still be discarded.

This paper discusses a method that combines the virtues of both the pictorial and spectral analyses. I model the calculated emittance spectra with Gaussian functions, which have only three parameters: a central wavelength, a standard deviation, and an amplitude. In principle, these may be displayed using color pictures. Because the displayed parameters are calculated from all six measured values, more information is displayed than in false-color pictures made from the acquired data. In this paper, I attempt to show that significant lithologic information is contained in these calculated parameters, and that they vary systematically with conventional measures of composition. The three parameters thus form a basis for quantitative photo-interpretation and lithologic mapping.

DATA ACQUISITION

TIMS Data

TIMS is a Daedalus airborne line-scanner operated by NASA on its NSTL Lear jet. TIMS acquires six channels of radiance (photon flux) data in spectral bands having peak sensitivities at 8.3, 8.7, 9.1, 9.8, 10.4, and $11.3 \mu\text{m}$, respectively. Details of the instrument are available in Palluconi and Meeks [1985].

During the summer of 1982 TIMS was flown over granitic rocks in the Sierra Nevada batholith, California, and again over the Josephine ophiolite in northern California and southern Oregon, acquiring data for a wide range of crystalline igneous silicate rocks. TIMS data acquired over Death Valley, California [Kahle and Walker, 1984] were used to augment these data. TIMS was flown near noon to maximize the thermal radiance and hence the signal/noise ratio. Data were provided to JPL by NASA/NSTL as computer-compatible tapes.

Ancillary Data

Thermal reflectance spectra were measured for representative rock samples collected in the field, on freshly broken and natural weathered surfaces. This was done at JPL using an Analect Fourier Transform Infrared Spectrometer. Spectra were averaged for roughly 25 locations on each rock sample, depending on grain size, to ensure that they represented the bulk rock composition and could be related to TIMS data collected over outcrop areas of ~400 m².

Estimates were made of the modal mineral abundances in selected samples by point counts of thin sections [Gillespie and Abbott, 1984]. SiO₂ content was measured by electron microprobe analysis of glass beads fused from powdered rock samples [e.g., Nash, 1964; Baldridge, 1979]. Results were checked against values calculated from the modal mineral abundances for the same samples.

DATA PROCESSING

TIMS Data

Calibration and Correction... The TIMS images were corrected for systematic panoramic distortions using a nearest-neighbor algorithm (not interpolation), to avoid further spectral mixing than was inherent in the data as acquired. The data were converted to units of photon flux, using the line-by-line internal blackbody reference or calibration values. Some additional aspects of required image processing are found in a companion paper [Gillespie, 1986]. After the data were corrected for instrument effects, emittance values were calculated for the six image channels, using a variation of the method of Kahle et al. [1980].

Calculating Emittances From TIMS Data... In order to calculate emittances from TIMS data, it is necessary to assume an emittance for one channel because there are seven unknowns (six emittances and the temperature) but only six radiance measurements. Based on this assumption, a model ground temperature can be calculated for each point in the image. Emittances for the other channels are then found from the measured photon flux ratioed to the flux predicted by Planck's Law for a blackbody at the model temperature. In this way, emittance images for all six channels were constructed from the acquired radiance images.

Kahle et al. [1980] assumed the emittance in channel 6 was always 0.93. This is valid for granites, but not for mafic and ultramafic rocks, which have low emittances near 11 μm . For these rocks the reststrahlen band lies at longer wavelengths than channel 1, and the emittance in channel 1 is more-or-less constant. Therefore, for granitic rocks the assumption of Kahle et al. [1980] was used, but for mafic and ultramafic rocks the

emittance in channel 1 was taken to be 0.98, a value that was measured for several samples on the Analect spectrometer. In the future a more elegant solution would be to calculate the apparent blackbody temperature for each TIMS channel; the channel for which the maximum temperature was found would be assigned an arbitrary emittance (e.g., 0.95), and the remaining emittances would be calculated as described above. It would be useful to create an image that reported the channel which had the maximum temperature, also. For this study, however, the simplified scheme in which either channel 1 or 6 was fixed was used.

Atmospheric Effects... The method of calculating emittances described above does not correct for atmospheric effects such as absorption and radiation by water vapor. While model corrections have been applied [Kahle et al., 1981], these depend on some knowledge of the air mass above the scene at the time of data acquisition. For the images used in this study, that vital information was lacking.

However, recent investigations with JPL's Portable Field Emission Spectrometer have shown that vegetation is spectrally flat in the 8-12 μm region. Any observed structure in the TIMS emittance spectra of vegetation is thus a measure of actual atmospheric effects. Therefore, atmospheric effects were reduced by normalizing the calculated emittances to values found for vegetation in the same scene. This approach is valid for multiplicative mixing (e.g., translucent atmosphere) but not for additive mixing (e.g., radiating atmosphere). It is valid only for a similar optical path through a single air mass; thus the target and the vegetation must be at similar scan angles and elevations, and must be viewed through the same mass of air. Water vapor affects primarily TIMS channel 1, whereas atmospheric ozone affects channel 4. The effect on channel 1 appears to be stronger and more variable than for channel 4.

Ultimately, it will be desirable to correct for both multiplicative and additive atmospheric effects. The iterative spectral mixing models of Adams et al. [1986] could probably be modified to do this. One of their advantages is that it is not necessary to completely describe the atmosphere in order to identify and remove its effects on the image spectra.

Sampling the Image Data... For this study, six-valued emittance spectra were extracted from the processed images for sites identified on an interactive image analysis station at JPL's Image Processing Laboratory. Sites were selected based on field experience and existing geologic maps [Moore, 1963; Cater and Wells, 1953; Harper, 1980, 1984] to represent all major rock types encountered in the scenes studied. They were chosen because they contained outcrops of rock larger than the ~20-m nadir pixels, no vegetation, and little soil.

Laboratory Spectra

Thermal infrared reflectance spectra were also obtained in the laboratory for rock samples collected at some sites identified in the TIMS images. Kahle et al. [1984] have demonstrated that, for remote observations of many natural rock surfaces, emittance and reflectance are strongly anticorrelated at thermal infrared wavelengths, and are in fact related through Kirchoff's Law:

$$\epsilon(\lambda) = 1 - r(\lambda) \quad (1)$$

where $\epsilon(\lambda)$ is the emissivity or emittance and $r(\lambda)$ is the reflectivity or reflectance at wavelength λ [e.g., Lyon, 1965]. Such is not the case for all samples, for example, powders and polished surfaces [Conel, 1969]. I calculated emittance spectra according to equation (1). TIMS emittance values were simulated from laboratory data by integrating the product of the calculated emittance spectra and the TIMS instrument response functions for the six channels.

Data Regression

All TIMS and simulated TIMS six-valued emittance spectra for the selected sites and rock types were fitted by Gaussian functions according to

$$\epsilon(\lambda) = 1 - \frac{A}{\sqrt{2\pi}} \exp \left[-\frac{1}{2} \left(\frac{\lambda - \lambda_c}{\sigma} \right)^2 \right] \quad (2)$$

where A is the amplitude, λ_c is the central wavelength and σ is the standard deviation. Note that in equation (2) the Gaussian function is actually related to $r(\lambda)$, not $\epsilon(\lambda)$. The fitting was done by linear regression on the cumulative distribution function of $(1-\epsilon(\lambda))$ values plotted, on a probability grid, against the peak wavelengths of the six spectral bands of TIMS. The central wavelength λ_c of the fitted function was found from the abscissa (λ) value for which the regressed line had an ordinate value (probability) of 0.5. The standard deviation was found from the difference between λ_c and the wavelength at which the probability was 0.68. The third parameter, the amplitude A of the fitted function, cannot be found in the above manner. Instead, A is taken to be the maximum difference found among the six calculated emittance values.

RESULTS

TIMS and Laboratory Spectra

Figures 1 through 5 show laboratory reflectance spectra and TIMS emittance spectra for fresh and weathered silicate rocks. Laboratory spectra for freshly broken samples are shown in Figure 1, plotted with reflectance increasing downward, to simulate emittance. All the samples came from the study areas, except the Eureka Quartzite, which was from the Death Valley data [Kahle and Walker, 1984]. Reflectances range from 1% to 79% with the maximum value (minimum emittance) occurring at different wavelengths from sample to sample, from 8.6 to 10.3 μm .

The orthoquartzite exhibited the greatest emittance (reflectance) contrast, with a double reststrahlen band from 8 to 9 μm which is characteristic of SiO_2 . This doublet is also prominent in the spectrum of the quartz-rich (28%) Bullfrog quartz monzonite, along with other bands attributable to feldspar and possibly clay minerals. These bands are found from 9 to 10 μm , and make the spectrum asymmetric. The maximum reflectance is ~37%, much less than for the Eureka Quartzite. This is probably due to the lower quartz content of the Bullfrog pluton and to the abundance of feldspar, which has less intense reststrahlen bands than quartz.

The spectrum of quartz-poor (7%) rocks, also from the Bullfrog pluton, shows the quartz bands subordinate to the feldspar bands, which have peak reflectances of only 12%. The spectrum of the hornblende diorite, which has only a trace of quartz, has even lower reflectances for $\lambda < \sim 9 \mu\text{m}$. The feldspar (plagioclase) band near 9.5 μm is still present, but the largest band is probably due to the hornblende, centered near $\sim 10.2 \mu\text{m}$.

Finally, the spectrum of the Josephine Peridotite has an intense band (38% contrast) near 9.5 μm , and a large shoulder near 11 μm . The dominant band is attributable to serpentine minerals; the smaller features are probably due to olivine.

Figure 2 contrasts laboratory reflectance spectra for freshly broken and natural weathered surfaces of the quartz-rich Bullfrog quartz monzonite and the serpentinized Josephine Peridotite of Figure 1. Weathered surfaces of both rock types are less than half as reflective as the fresh surfaces in the reststrahlen bands. Surprisingly, the contrast in quartz bands is reduced proportionately more than the bands at longer wavelengths, for the quartz monzonite. We tentatively attribute this to the presence of a thin clay coat on the weathered surface. Reststrahlen bands for the clay minerals from 9 to 10 μm would keep contrast high there.

Contrast for the weathered peridotite is reduced even more than for the quartz monzonite. A broad feature is still evident at 10 μm , however. Apparently, the serpentine minerals are not preserved on the weathered surface, which consists primarily of Fe oxides, orthopyroxene, and minor olivine.

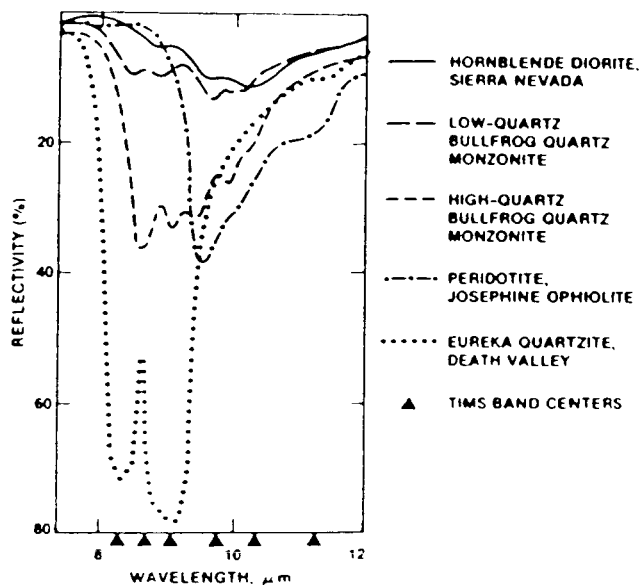


Figure 1. Laboratory reflectance spectra of fresh silicate rocks (reflectance increases downward).

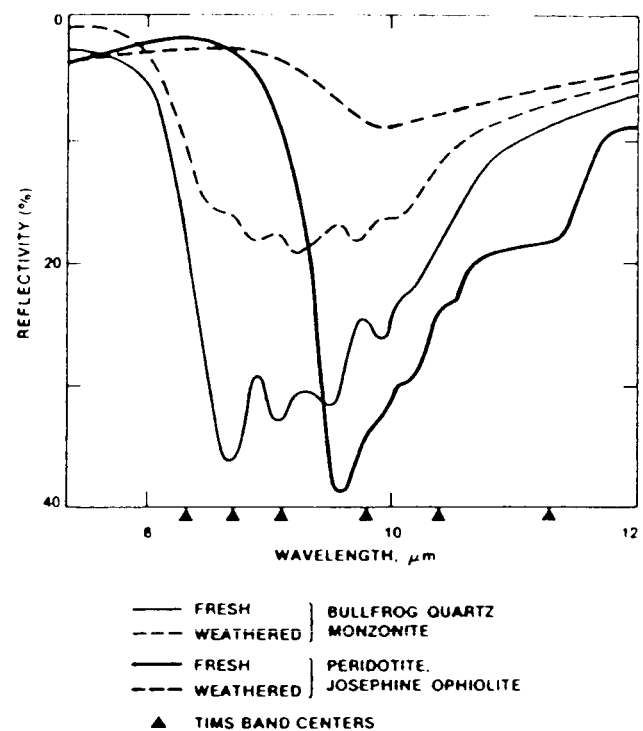


Figure 2. Laboratory reflectance spectra of fresh and weathered rocks

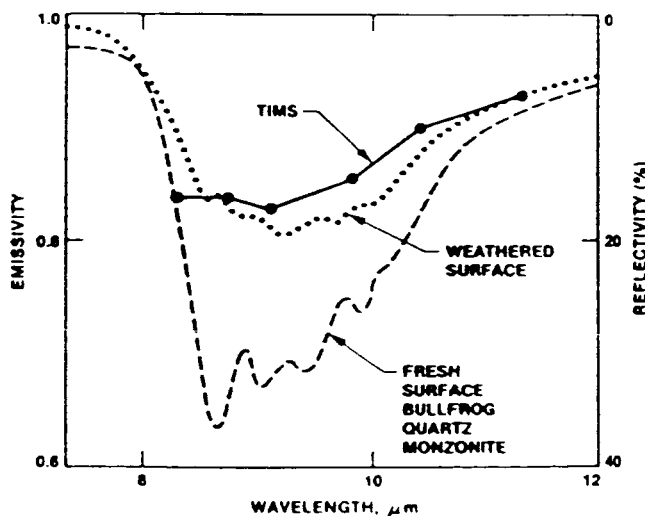


Figure 3. Laboratory reflectance spectra of freshly broken and natural weathered surfaces of Bullfrog quartz monzonite compared to emittance spectra calculated from TIMS

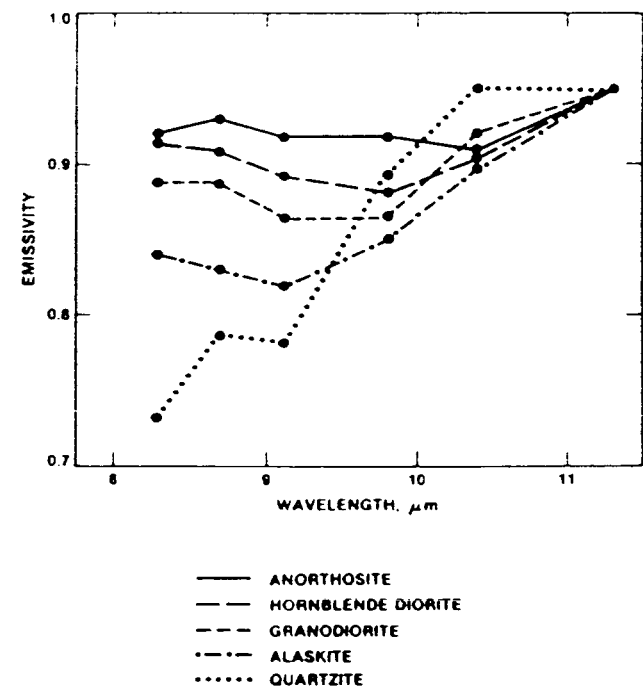


Figure 4. TIMS emittance spectra of silicate rocks ($\epsilon_0 = 0.95$). The quartzite spectrum was not corrected for atmospheric effects.

Figure 2 emphasizes that remotely sensed images show natural surfaces that are not compositionally the same as the fresh bedrock. Nevertheless, weathering is not necessarily so intense that bedrock composition cannot be inferred.

Figure 3 compares the TIMS emittance spectrum for an outcrop of the quartzose facies of the Bullfrog pluton to the laboratory reflectivity spectra of fresh and weathered surfaces. Clearly, the TIMS spectrum does not resemble the spectrum of the fresh surface, but it is similar to the spectrum of the weathered surface. Even so, the emittance for TIMS channel 1 appears to be somewhat too low. Perhaps this is due to incomplete correction for atmospheric water, which affects channel 1 most strongly. It is also possible that the disagreement arises from an incorrect choice of the model emittance for channel 6. To first order, this would introduce a gradient in the apparent spectrum, because of the non-linear nature of the Planck function.

Figure 3 reinforces the findings of Kahle et al. [1984], and demonstrates that TIMS emittances and the laboratory reflectance spectra used in this study are in fact related through Kirchoff's law (equation 1).

Figure 4 presents five TIMS emittance spectra for different silicate rock types. As in Figure 1, the Eureka Quartzite spectrum has the highest contrast. The emittance for TIMS channel 1 is lower than expected from the spectrum of the quartzite, which we attribute to atmospheric water. Kahle and Walker [1984] did not correct the quartzite spectrum for atmospheric effects by the method described here, because of the absence of vegetation in Death Valley. The minimum emittance of 0.22 for the other channels is considerably less than the value of 0.77 predicted by Kirchoff's Law for the fresh quartzite. Perhaps this is due to a thin film of desert varnish of the natural weathered surface. Even so, the quartzite spectrum has more contrast than those for the igneous silicate rocks.

The spectra of the igneous silicate rocks show a decrease in contrast and an increase in the wavelength at which the minimum emittance is found as the composition becomes more mafic, as expected.

Figure 5 shows TIMS emittance spectra for serpentinitized Josephine Peridotite and for lateritic soils developed over the peridotite. The soil spectrum is nearly flat, a result corroborated by data from the JPL Portable Field Emission Spectrometer. The peridotite spectra differ from the laterite and from each other primarily in channels 4 and 5 (9.8 and 10.3 μm). In Figure 5 it is evident that a false-color picture of the kind used in most early studies of TIMS data, based on channels 1, 3, and 5, would discriminate between the fresh and weathered rock poorly, because channel 4 was discarded. This emphasizes the need to examine all six image channels in lithologic mapping.

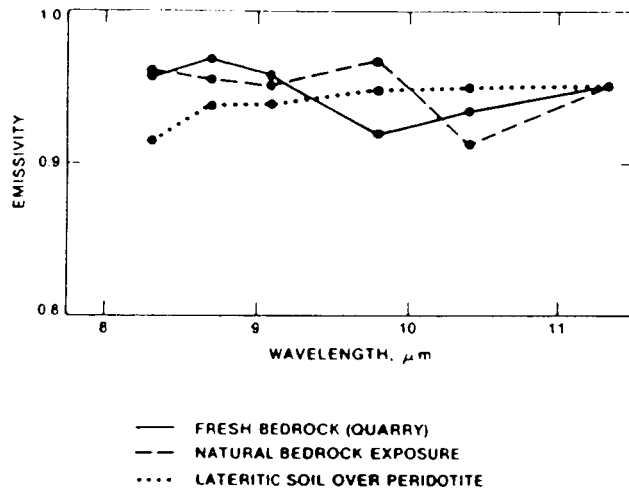


Figure 5. TIMS emittance spectra for Josephine Peridotite and lateritic soils in northern California. The emittance for Channel 6 was set to 0.95 for comparison to Fig. 4.

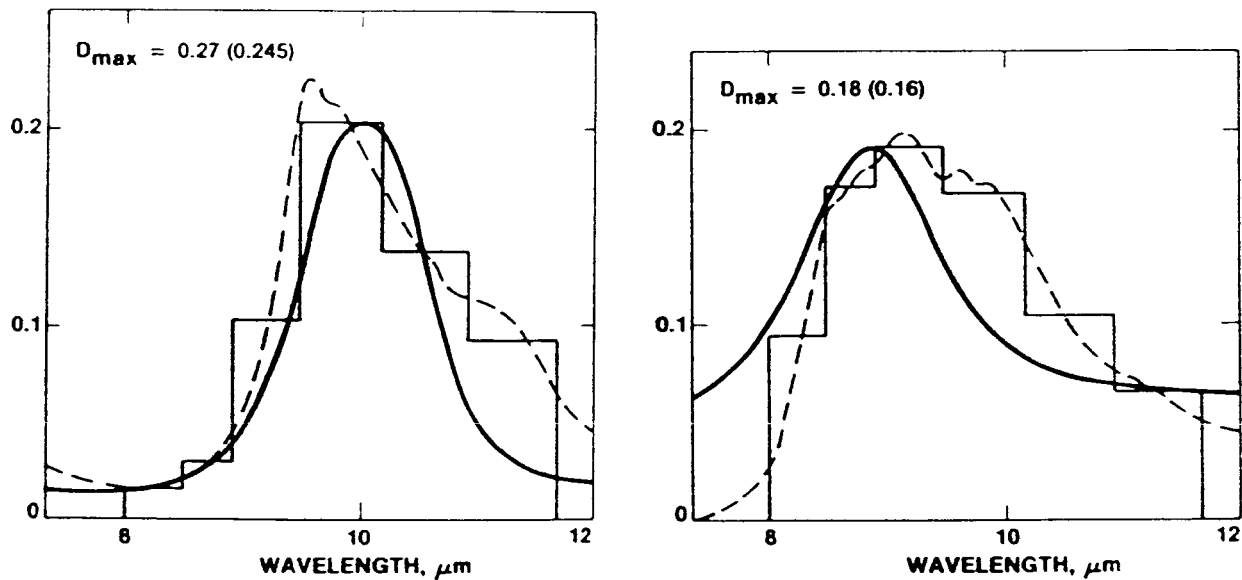


Figure 6. Continuous laboratory reflectance spectra (dashed line), simulated TIMS emittance spectra (light solid line), and Gaussian functions fitted to TIMS spectra (heavy solid line). Left figure is for serpentinized peridotite; right figure is for quartz monzonite. Kolmogorov-Smirnov test statistic is in the upper left-hand corner. Parenthetical values are calculated for reflectance vs λ^{-1} .

Figure 5 shows that soils developed atop bedrock need not resemble the unweathered substrate at all. However, it should be possible to discriminate between soil and bedrock, and even to estimate the degree and weathering on bedrock outcrops.

Fitting Gaussian Functions to TIMS Data

Figures 6 through 9 describe the regression of normal functions to the emittance spectra and show the relationship among the three parameters of the fitted curves: A , λ_c and σ . Figure 6 shows laboratory reflectance spectra, simulated TIMS data and the curves fitted to them for peridotite and quartz monzonite. For peridotite, the continuous spectrum is simple, and the assumption that it may be fitted by a Gaussian function appears to be realistic. The continuous spectrum for the quartz monzonite contains several distinct features, and will be less well described by a Gaussian function. However, the complexity is not evident in the TIMS spectrum, which is severely undersampled.

The normality of the TIMS spectra was tested with the one-sample Kolmogorov-Smirnov test [e.g., Bradley, 1968; Till, 1974], using the modified tables of Lilliefors [1967] that apply when the population is unknown. The test results show that the hypothesis that the TIMS spectra are normal cannot be rejected at the 80% confidence level. Fitting curves according to wavenumber rather than wavelength did not appreciably improve the fit. The use of normal curves to describe the six-valued TIMS spectra is probably justified, although this might not be true for image data having higher spectral resolution and more channels.

Figure 7 presents a variation diagram relating A (emittance contrast) and λ_c (central wavelength) for normal functions fitted to TIMS emittance spectra for various silicate rocks. The data loosely follow a trajectory in this diagram, according to lithology. A general dispersion of rock types with λ_c is more pronounced than with A . It appears that A decreases as λ_c increases for granitic rocks, but for mafic and ultramafic rocks A is unchanged over a 0.6- μm range of λ_c . These results are predictable from the laboratory data presented above. However, the scatter of data - especially along the A axis - may arise in part from natural variability of weathered surfaces in the TIMS data. In particular, minor amounts of vegetation, including lichens, will strongly affect A .

Figure 8 shows the effect of spectral mixing between bedrock and vegetation (blackbody or graybody spectrum) in TIMS data. The emittance contrast in the spectrum for quartz monzonite is progressively reduced with increasing vegetative cover. This effect is noticeable for as little as 5% cover and profoundly influences the parameter A . There appears to be little effect on the shape of the spectra; therefore, we expect σ and λ_c to be less sensitive than A to partial vegetation cover.

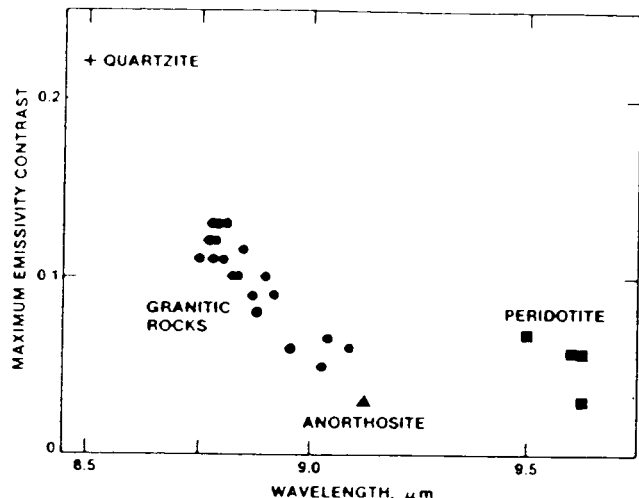


Figure 7. Variation diagram relating A (maximum emittance contrast) and λ_c (central wavelength) for TIMS emittance spectra for various silicate rocks.

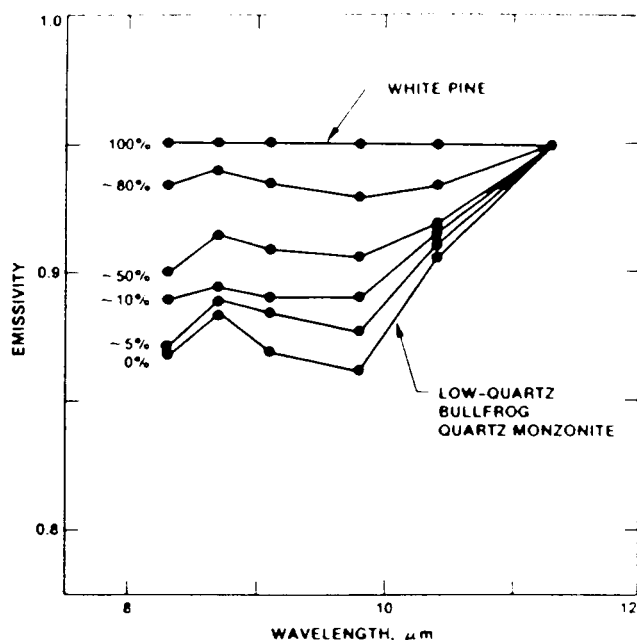


Figure 8. TIMS emittance spectra for rocks of the Bullfrog pluton (Sierra Nevada) under partial vegetation cover (shown to the left of the spectra).

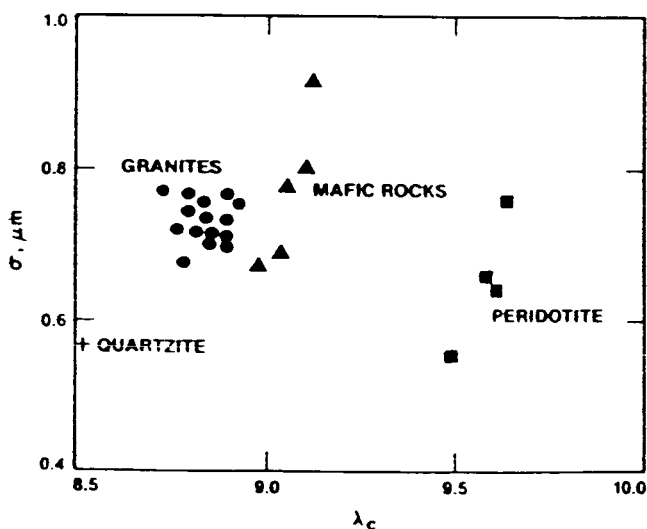


Figure 9. Variation diagram relating regression parameters σ (standard deviation) and λ_c for TIMS emittance spectra of various silicate rocks.

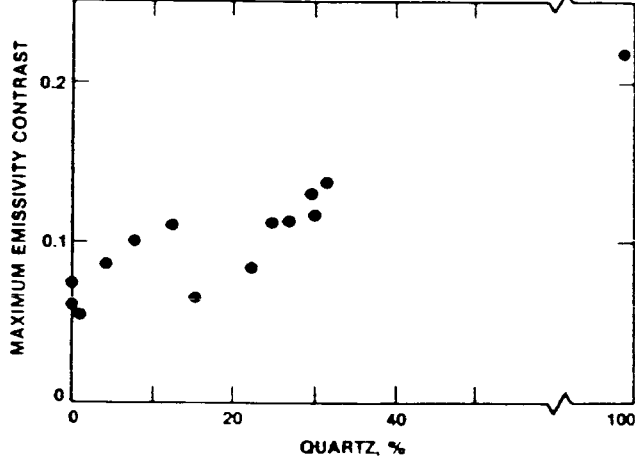


Figure 10. Variation in A (maximum emittance contrast) with modal quartz in simulated TIMS spectra of various silicate rocks, calculated from laboratory reflectance spectra.

It is important to recognize that, in general, spectral mixing in thermal IR images can be quite complicated, even if it is limited to binary mixing between only two endmembers or components. Not only do the emittance spectra characteristic of the endmembers radiating to the sensor differ, but the temperatures at which they radiate may also. Because of the exponential temperature dependence of radiance in Planck's Law, the effect of temperature differences can be profound. At the least, it implies that a particular mixed spectrum can be achieved by quite a range of endmember concentrations or fractions. Further complications are introduced because the shape of the blackbody spectrum is also temperature-dependent. Thus it is non-trivial to estimate the fraction of vegetation cover, for example, from thermal infrared data. Despite this, Figure 8 demonstrates that it is possible to detect the presence of mixing in a straightforward manner.

Figure 9 shows the relationship between the regression parameters σ and λ_e for various silicate rocks. Although σ ranges from 0.6 to 0.9, there is no obvious correlation with λ_e . We note that σ is smallest for the monomineralic quartzite and for one of the peridotite samples. Granitic and especially mafic rocks have larger values of σ . Probably σ is larger for rocks containing several minerals, and hence for complicated spectra containing reststrahlen bands at two or more wavelengths. Thus σ , like A, may be sensitive to spectral mixing.

Regression Parameters and Rock Composition

Figures 10 through 12 show how the parameters A and λ_e vary with two conventional measures of rock composition: modal quartz and silica abundance. Figure 10 relates A and modal quartz abundance. As suggested from Figure 7, there is a pronounced positive correlation. The value of A ranges from ~0.07 for rocks with no quartz to ~0.16 for granitic rocks with 30% quartz. For the Eureka Quartzite, A is 0.22. The parameter A is clearly controlled in part by the intense quartz reststrahlen bands. As seen in Figure 8, in most image data A will also be controlled by vegetative cover, thus complicating its interpretation.

Figure 11 illustrates the covariation of λ_e and modal quartz. λ_e decreases from 9.7 to 8.5 μm as quartz content rises from 0 to 100%. Half that variation occurs for quartz-free rock types. Ultramafic, mafic and granitic rocks and quartzite are all separable by λ_e . The discrimination of the peridotites and quartz-free diorites shows that λ_e is not sensitive to quartz alone.

Figure 12 illustrates the correlation of λ_e and silica abundance for the same rock types as Figure 11. It is important to emphasize that λ_e is not responding to silica content *per se*; rather, it is responding to the succession of minerals that occurs with increasing silica in igneous rocks. Low-silica rocks contain olivine and pyroxene, both of which have reststrahlen bands near 10 μm . Rocks with more silica contain amphibole and feldspar,

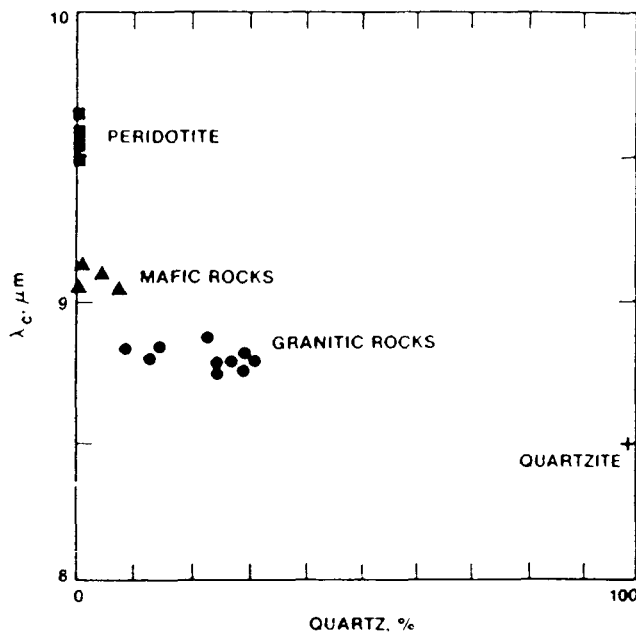


Figure 11. Variation in λ_c (central wavelength) with modal quartz for TIMS emittance spectra of various silicate rocks.

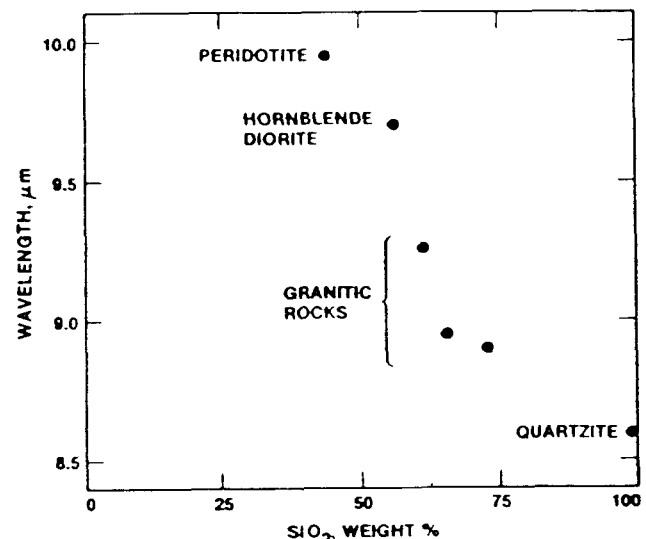


Figure 12. Variation in λ_c (central wavelength) with silica content for simulated TIMS spectra of various silicate rocks, calculated from laboratory reflectance spectra.

which have bands from 9 to 10 μm . High-silica rocks have feldspar and quartz which has bands from 8 to 9 μm . Because silica content is a basis for the classification of igneous rocks, it is useful to note the indirect correlation of λ_c and silica abundance.

The simple relationship between λ_c and modal quartz or silica and the separability of common igneous rock types establishes regression of normal or other appropriate functions on TIMS emittance spectra as a useful tool for the construction of images for photointerpretation. In particular, strong inferences about rock type can be made from λ_c , so images of λ_c will be an aid in lithologic mapping. Addition of Δ and σ images, along with λ_c , as elements in false-color pictures would increase the amount of information available to the photointerpreter.

SUMMARY

Six-channel emittance images were calculated from radiance images acquired in the spectral region 8-12 μm by the NASA airborne Thermal Multispectral Infrared Scanner (TIMS) over the Sierra Nevada batholith and over the Josephine ophiolite in California. The apparent emittances were fitted by Gaussian functions

intended to model the reststrahlen bands in the emittance spectra. Thus the information contained in the original six-channel image was, in a sense, "compressed" to three channels representing the width, amplitude, and central wavelength of the Gaussian function. The width was greater for multimineralic rocks and appeared to be sensitive to mixing of mineral or rock types. Contrast was especially sensitive to quartz content. The central wavelength was correlated to modal quartz abundances found from thin sections and to silica abundances measured by microprobe analyses of rock samples from selected outcrops representing a range of rock types. It was the best single measure of rock composition. Peridotites, hornblende diorites, granodiorites and quartz monzonites were all separable by the regression parameters.

Vegetative cover as low as 5% influenced the apparent emittances, and especially the contrast in the spectrum. Yet, because vegetation radiates like a blackbody or a graybody, spectral mixing of radiation from vegetation and a substrate does not generally obscure features of the emittance spectrum of the substrate, except for contrast.

Thermal image data appear to be a valuable adjunct to field techniques in geologic mapping of silicate rocks. They augment aerial photographs and near-infrared images in that they depict differences in silicate minerals composing the rocks, not just in the color index, the degree of oxidation, or the extent of hydration.

ACKNOWLEDGEMENTS

NSTL personnel, particularly G. Meeks, have been unstinting in their support, operation, and improvement of TIMS. E. Abbott did the thin section analyses. The research described in this paper was carried out at the Jet Propulsion Laboratory of the California Institute of Technology and sponsored by the Earth Processes Branch of the National Aeronautics and Space Administration.

REFERENCES CITED

- Adams, J.B., M.O. Smith and P.E. Johnson, 1986, Viking Lander I: A new map of rock and soil types, *Jour. Geophys. Res.*, in press.
- Baldridge, W.S., 1979, Petrology and Petrogenesis of Basaltic Rocks and Their Inclusions: Studies from the Rio Grande Rift, the Roman Comagmatic Province, and Mare Procellarum, Ph.D. Thesis, California Institute of Technology, 324 pp.
- Bradley, J.V., 1968, Distribution-Free Statistical Tests, Prentice-Hall, Englewood Cliffs, New Jersey, 388 pp.

A.R. Gillespie: Mapping Silicate Rocks...

Cater, F.W. Jr. and F.G. Wells, 1953, Geology and Mineral Resources of the Gasquet Quadrangle, California - Oregon, Geological Survey Bull. 995-C, 133 pp.

Conel, J., 1969, Infrared Emissivities of Silicates: Experimental Results and a Cloudy Atmosphere Model of Spectral Emission from Condensed Particulate Mediums, *Jour. Geophys. Res.*, 74, 1614-1634.

Gillespie, A.R., 1986, Enhancement of TIMS images for photointerpretation, this volume.

Gillespie, A.R., and E.A. Abbott, 1984, Mapping compositional differences in silicate rocks with six-channel thermal images, *Proc. 9th Canadian Symposium on Remote Sensing*, St. John's, Newfoundland, Aug., 327-336.

Gillespie, A.R., A.B. Kahle and R.E. Walker, 1986, Color enhancement of highly correlated images: I. Decorrelation and HSI stretches, *Remote Sensing of Environment*, in press.

Harper, G.D., 1980, The Josephine Ophiolite - Remains of a Late Jurassic Marginal Basin in Northwestern California, *Geology*, 8, 333-337.

Harper, G.D., 1984, The Josephine Ophiolite, Northwestern California, *Geol. Am. Soc. Bull.*, 95, 1009-1026.

Hunt, G.R., 1980, Electromagnetic Radiation: the Communication Link in Remote Sensing, in Siegal, B.S., and A.R. Gillespie, eds., Remote Sensing in Geology, Wiley, New York, pp 5-45.

Hunt, G.R. and J.W. Salisbury, 1974, Mid-Infrared Spectral Behavior of Igneous Rocks, Air Force Cambridge Lab. Tech. Rept. (AFCRL-TR-74-0625.)

Kahle, A.B. and L.C. Rowan, 1980, Evaluation of Multispectral Middle Infrared Aircraft Images for Lithologic Mapping in East Tintic Mountains, Utah, *Geol.*, 8, 234-239.

Kahle, A.B., and R.E. Walker, 1984, Calculation of emissivity and thermal inertia at Death Valley, California, from TIMS data, *Proc. 9th Canadian Symposium on Remote Sensing*, St. John's, Newfoundland, Aug., 337-346.

Kahle, A.B., D.P. Madura and J.M. Soha, 1980, Middle Infrared Multispectral Aircraft Scanner Data: Analysis for Geological Applications, *Appl. Optics*, 19, 2279-2290.

Kahle, A.B., J.P. Schieldge, M.J. Abrams, R.E. Alley and C.J. Levine, 1981, Geologic Application of Thermal Inertia Imaging Using HCMM Data, *JPL Publication 81-55*, 199 pp.

Kahle, A.B., M.S. Shumate and D.B. Nash, 1984, Active Airborne Infrared Laser System for Identification of Surface Rocks and Minerals, *Geophys. Res. Lett.*, 11, 1149-1152.

Lilliefors, H.W., 1967, On the Kolmogorov-Smirnov Test for Normality with Mean and Variance Unknown, *Jour. Amer. Stat. Assn.*, 62, 399-402.

A.R. Gillespie: Mapping Silicate Rocks...

Lyon, R.J.P., 1965, Analysis of Rocks by Spectral Infrared Emission (8 to 25 Microns), Econ. Geol., 60, 715-736.

Moore, J.G., 1963, Geology of the Mount Pinchot Quadrangle, Southern Sierra Nevada, California, U.S. Geol. Survey Bull. 1130, 152 pp.

Nash, D.B., 1964, New Technique for Quantitative SiO₂ Determinations of Silicate Materials by X-Ray Diffraction Analysis of Glass, in Mueller, W.M., G.R. Mallett and M.J. Fay, eds., Advances in X-Ray Analysis, 7, Plenum Press, New York, pp 209-228.

Palluconi, F.D., and G.R. Meeks, 1985, Thermal Infrared Multispectral Scanner (TIMS): An investigator's guide to TIMS data, JPL Publication 85-32, Jet Propulsion Laboratory, Calif. Inst. Technology, Pasadena, CA, 22 pp.

Soha, J.M. and A.A. Schwartz, 1978, Multispectral Histogram Normalization Contrast Enhancement, Proc. 5th Canadian Symposium on Remote Sensing, Victoria, B.C., pp 86-93.

Till, R., 1974, Statistical Methods For The Earth Scientist, Wiley, New York, 154 pp.

Vincent, R.K., F. Thomson and K. Watson, 1972, Recognition of Exposed Quartz Sand and Sandstone by Two-Channel Infrared Imagery, Jour. Geophys. Res., 77, 2473-2477.

* * * * *